Internal Modes of Multidecadal Variability in the Arctic Ocean

LEELA M. FRANKCOMBE AND HENK A. DIJKSTRA

Institute for Marine and Atmospheric Research Utrecht, Utrecht University, Utrecht, Netherlands

(Manuscript received 14 April 2010, in final form 17 June 2010)

ABSTRACT

Observations of sea ice extent and atmospheric temperature in the Arctic, although sparse, indicate variability on multidecadal time scales. A recent analysis of one of the global climate models [the Geophysical Fluid Dynamics Laboratory Climate Model, version 2.1 (CM2.1)] in the Fourth Assessment Report (AR4) of the Intergovernmental Panel on Climate Change has indicated that Arctic Ocean variability on these time scales is associated with changes in basin-wide salinity patterns. In this paper the internal modes of variability in an idealized Arctic Basin are determined by considering the stability of salinity-driven flows. An internal ocean mode with a multidecadal time scale is found, with a spatial pattern similar to that obtained in the analysis of the CM2.1 results. The modes propagate as a ''saline Rossby wave'' induced by the background salinity gradient.

1. Introduction

Natural variability of the climate of the Arctic Ocean on decadal to multidecadal time scales is a topic that has recently begun to receive a large amount of attention. Anthropogenic climate change appears to be having its greatest effects in the Arctic, yet we have so far been unable to accurately predict the rates of the changes using state-of-the-art climate models (Stroeve et al. 2007). The 2007 minimum in sea ice extent, for example, was not adequately projected by any of the models in the Intergovernmental Panel on Climate Change's Fourth Assessment Report (AR4). This prompts the question as to whether natural variability may be enhancing anthropogenically induced changes and, if so, what mechanisms may be responsible.

The study of multidecadal variability in the North Atlantic Ocean also leads to questions about variability in the Arctic. Temperature and salinity anomalies from the North Atlantic may propagate into the Arctic and vice versa, connecting variability in the two basins. Long-term observations in the Arctic region are limited; however, there are indications of decadal-to-multidecadal variability in air pressure and temperature (Polyakov et al. 2003a), sea ice (Polyakov et al. 2003b), and temperature of Atlantic core water entering the Arctic (Polyakov et al. 2004). Multidecadal variability in century-long records of sea ice is found to be strongest in the Kara Sea, decaying toward the Canada Basin (Venegas and Mysak 2000; Polyakov et al. 2003b). This multidecadal variability has been referred to as the low-frequency oscillation (Polyakov and Johnson 2000). There are also multidecadal variations in sea ice transport through Fram Strait associated with the variability of sea ice extent (Vinje et al. 2002). In addition, there are the Great Salinity Anomalies (GSAs) in the North Atlantic, of which several are thought to be connected to large sea ice exports out of the Arctic (Belkin et al. 1998).

Another connection between the North Atlantic and Arctic climate occurs through the atmosphere. The dominant atmospheric winter variability is associated with the pattern of the North Atlantic Oscillation (NAO), with its Arctic extension, the Northern Annular Mode (Thompson and Wallace 2001). Although it cannot be demonstrated that the NAO has any significant preferential frequency, the Atlantic westerlies were relatively weak during the period between 1940 and 1970 and relatively strong from 1980 until recently (Eden and Jung 2001). NAO variations impose a well-known tripolar sea surface temperature anomaly on the North Atlantic Ocean on seasonal to interannual time scales (Alvarez-Garcia et al. 2008), while a hemisphere-wide

Corresponding author address: Leela M. Frankcombe, Institute for Marine and Atmospheric Research Utrecht, Dept. of Physics and Astronomy, Utrecht University, Princetonplein 5, 3584 CC Utrecht, Netherlands.
E-mail: l.m.frankcombe@uu.nl

DOI: 10.1175/2010JPO4487.1

response is associated with low-frequency time scales (Visbeck et al. 2003).

Frankcombe et al. (2010) found multidecadal variability in the North Atlantic on two time scales and proposed that the shorter 20–30-yr time scale arises due to an ocean mode intrinsic to the North Atlantic basin (te Raa and Dijkstra 2002), while the longer 50–70-yr time scale is associated with Arctic variability. Based on observations and an analysis of a 500-yr-long control run of the Geophysical Fluid Dynamics Laboratory's (GFDL) Climate Model, version 2.1 (CM2.1), they find that the source of the 50–70-yr period variability is an oscillation seen in salinity at 400-m depth in the Arctic. Note that 400 m is the approximate depth of the layer of Atlantic water in the Arctic. They suggested that the inflow from the Atlantic may be exciting an internal ocean mode in the Arctic Basin, which, in turn, feeds buoyancy anomalies back into the North Atlantic on the longer time scale. The salinity signatures of these anomalies may be related to GSAs, which would consequently be due to the internal multidecadal variability of the Arctic.

In this paper we take the first step toward determining the salinity-related internal multidecadal variability in the Arctic. The temperature-related internal modes of variability in the North Atlantic were studied in Dijkstra (2006) by considering the linear stability of thermally driven three-dimensional ocean flows in an idealized single-hemispheric basin. Under zero forcing, it was shown that the normal modes of the motionless state are stationary. With an increasing equator-to-pole temperature gradient, the growth rates of these modes are affected by the strength of the meridional overturning circulation, and some of the stationary modes merge to become oscillatory modes that, under realistic forcing, have multidecadal periods. Following the approach in Dijkstra (2006), we can immediately anticipate that if we consider salinity-driven flow in an idealized Arctic Basin, mergers of stationary modes may also occur. The issue, however, is whether they will have a multidecadal period and whether the patterns of these modes will correspond to those found in the GFDL CM2.1 results (Frankcombe et al. 2010).

In section 2, the model and methodology used to determine the internal modes for a hierarchy of idealized Arctic Ocean models are presented. In section 3, results are presented for a circular basin with a polar island and it is shown that both westward- and eastward-propagating multidecadal modes exist. In section 4, we analyze the effects of geometry and idealized bottom topography on the modes. We summarize the results in section 5 and discuss them within the context of the results of general circulation models and observations.

2. Stability of Arctic Ocean flows

In section 2a we present the model used to address the internal variability in the Arctic, and in section 2b we present the methodology by which internal modes of variability are computed.

a. Ocean model

We consider ocean flows in a model domain on the sphere bounded by the latitudes θ_s and θ_n (to be specified later) and by the longitudes $\phi_w = 0°$ and $\phi_e = 360°$; the ocean basin has a mean depth D. The flows in this domain are forced by restoring surface boundary conditions (with a restoring time scale τ_S) to a salinity field S_R given by

$$S_R = S_0 + \Delta S f(\phi, \theta),$$

where ΔS is the amplitude of the salinity anomaly over the basin and $f(\phi, \theta)$ is a prescribed spatial pattern. The temperature and wind forcing are absent.

Salinity differences in the ocean cause density differences according to

$$\rho = \rho_0[1 + \alpha_S(S_* - S_0)],$$

where α_S is the volumetric expansion coefficient; S_0 and ρ_0 are a reference salinity and density, respectively; and S_* is the total salinity. We neglect inertia in the momentum equations because of the small Rossby number and use the Boussinesq and hydrostatic approximations. With r_0 and Ω being the radius and angular velocity of the earth, the governing equations for the zonal, meridional, and vertical velocities u, v, and w, respectively; the dynamic pressure p (the hydrostatic part has been subtracted); and the salinity $S = S_* - S_0$ become

$$-2\Omega v \sin\theta + \frac{1}{\rho_0 r_0 \cos\theta}\frac{\partial p}{\partial \phi} = A_V \frac{\partial^2 u}{\partial z^2} + A_H L_u(u, v), \quad (1a)$$

$$2\Omega u \sin\theta + \frac{1}{\rho_0 r_0}\frac{\partial p}{\partial \theta} = A_V \frac{\partial^2 v}{\partial z^2} + A_H L_v(u, v), \quad (1b)$$

$$\frac{\partial p}{\partial z} = -\rho_0 g \alpha_S S, \quad (1c)$$

$$\frac{1}{r_0 \cos\theta}\left[\frac{\partial u}{\partial \phi} + \frac{\partial (v\cos\theta)}{\partial \theta}\right] + \frac{\partial w}{\partial z} = 0, \quad \text{and} \quad (1d)$$

$$\frac{DS}{dt} - \nabla_H \cdot (K_H \nabla_H S) - \frac{\partial}{\partial z}\left(K_V \frac{\partial S}{\partial z}\right) = \frac{[\Delta S f(\phi, \theta) - S]}{\tau_S}\mathcal{H}\left(\frac{z}{H_m} + 1\right), \quad (1e)$$

TABLE 1. Standard values of parameters used in the numerical calculations.

$2\Omega = 1.4 \times 10^{-4}$ (s^{-1})	$r_0 = 6.4 \times 10^6$ (m)
$D = 4.0 \times 10^3$ (m)	$\tau_S = 7.5 \times 10^1$ (days)
$\alpha_S = 7.6 \times 10^{-4}$ (psu^{-1})	$H_m = 250$ (m)
$A_H = 1.6 \times 10^5$ ($m^2\ s^{-1}$)	$S_0 = 35.0$ (psu)
$\rho_0 = 1.0 \times 10^3$ ($kg\ m^{-3}$)	$A_V = 1.0 \times 10^{-3}$ ($m^2\ s^{-1}$)
$K_H = 1.0 \times 10^3$ ($m^2\ s^{-1}$)	$K_V = 2.3 \times 10^{-4}$ ($m^2\ s^{-1}$)

where $\mathcal{H}$ is a continuous approximation of the Heaviside function and H_m is the depth of the first layer. In these equations, A_H and A_V are the horizontal and vertical momentum (eddy) viscosities and K_H and K_V are the horizontal and vertical (eddy) diffusivities of salt, respectively. In addition,

$$\frac{D}{dt} = \frac{\partial}{\partial t} + \frac{u}{r_0\cos\theta}\frac{\partial}{\partial\phi} + \frac{v}{r_0}\frac{\partial}{\partial\theta} + w\frac{\partial}{\partial z}$$

$$\nabla_H \cdot (K_H \nabla_H) = \frac{1}{r_0^2\cos\theta}\left[\frac{\partial}{\partial\phi}\left(\frac{K_H}{\cos\theta}\frac{\partial}{\partial\phi}\right) + \frac{\partial}{\partial\theta}\left(K_H\cos\theta\frac{\partial}{\partial\theta}\right)\right]$$

$$L_u(u, v) = \nabla_H^2 u + \frac{u\cos 2\theta}{r_0^2\cos^2\theta} - \frac{2\sin\theta}{r_0^2\cos^2\theta}\frac{\partial v}{\partial\phi}$$

and

$$L_v(u, v) = \nabla_H^2 v + \frac{v\cos 2\theta}{r_0^2\cos^2\theta} + \frac{2\sin\theta}{r_0^2\cos^2\theta}\frac{\partial u}{\partial\phi}.$$

To remove any static instabilities, enhanced vertical mixing was applied when the vertical density gradient was positive. The implementation details of the convective adjustment scheme used in the model are provided in De Niet et al. (2007).

Slip conditions and zero salt flux are assumed at the bottom boundary and, as the forcing is represented as a body force over the first layer, slip and zero salt flux conditions also apply at the ocean surface. Hence, the boundary conditions at the top and bottom boundaries are

$$z = -D, 0: \quad \frac{\partial u}{\partial z} = \frac{\partial v}{\partial z} = w = \frac{\partial S}{\partial z} = 0. \tag{2}$$

The lateral boundary conditions will be specified in each of the different cases below. The parameters for the standard case are the same as in typical large-scale low-resolution ocean general circulation models and their values are listed in Table 1.

b. Steady states and their stability versus ΔS

Using the model in the previous subsection, we will compute steady three-dimensional salinity-driven flow solutions for different amplitudes of the surface salinity gradient ΔS and determine their linear stability.

First, the steady governing equations (1) and boundary conditions (2) are discretized on an Arakawa B grid using central spatial differences. On an $N \times M \times L$ grid with five unknowns per point (u, v, w, p, and S), this leads to a system of $d = 5 \times N \times M \times L$ nonlinear algebraic equations. These are solved with ΔS as a control parameter using a pseudoarclength continuation method; details on this methodology are provided in Dijkstra (2005).

For each of the steady states, we now consider the evolution of infinitesimally small disturbances within the model. Linearizing (1) and (2) in the amplitude of the perturbations and separating the equations for these disturbances in time, an elliptic eigenvalue problem is obtained for the complex growth rate σ of each perturbation. When this elliptic eigenvalue problem is discretized, a generalized eigenvalue problem is obtained of the form

$$\mathcal{A}\mathbf{x} = \sigma\mathcal{B}\mathbf{x}, \tag{3}$$

where $\mathcal{A}$ and $\mathcal{B}$ are $d \times d$ matrices. The matrix $\mathcal{A}$ is the Jacobian matrix of the system of nonlinear algebraic equations that results after the discretization of (1). The matrix $\mathcal{B}$ is singular since a time derivative only occurs in the salinity equation and is absent from the momentum equations and the continuity equation.

We solve for the 12 ''most dangerous'' modes, that is, those with their real part closest to the imaginary axis,

TABLE 2. Growth rates (yr^{-1}) of the least damped modes for different values of θ_n and K_V.

			$K_V = 2.3 \times 10^{-4}\ m^2\ s^{-1}$			$K_V = 1.0 \times 10^{-4}\ m^2\ s^{-1}$
n	m	l	90°N (analytic)	87.5°N (analytic)	87.5°N (model)	87.5°N (analytic)
0	0	1	-4.4742×10^{-3}	-4.4742×10^{-3}	-4.5043×10^{-3}	-1.9453×10^{-3}
0	0	2	-1.7897×10^{-2}	-1.7897×10^{-2}	-1.7843×10^{-2}	-7.7812×10^{-3}
1	0	0	-2.1708×10^{-2}	-2.0161×10^{-2}	-2.0814×10^{-2}	-2.0161×10^{-2}
1	0	1	-2.6182×10^{-2}	-2.4635×10^{-2}	-2.5319×10^{-2}	-2.2106×10^{-2}
1	0	2	-3.9605×10^{-2}	-3.8058×10^{-2}	-3.8658×10^{-2}	-2.7942×10^{-2}
0	0	3	-4.0268×10^{-2}	-4.0268×10^{-2}	-3.9506×10^{-2}	-1.7508×10^{-2}
2	0	0	-6.0332×10^{-2}	-6.0111×10^{-2}	-6.1145×10^{-2}	-6.0111×10^{-2}
1	0	3	-6.1976×10^{-2}	-6.0429×10^{-2}	-6.0321×10^{-2}	-3.7669×10^{-2}

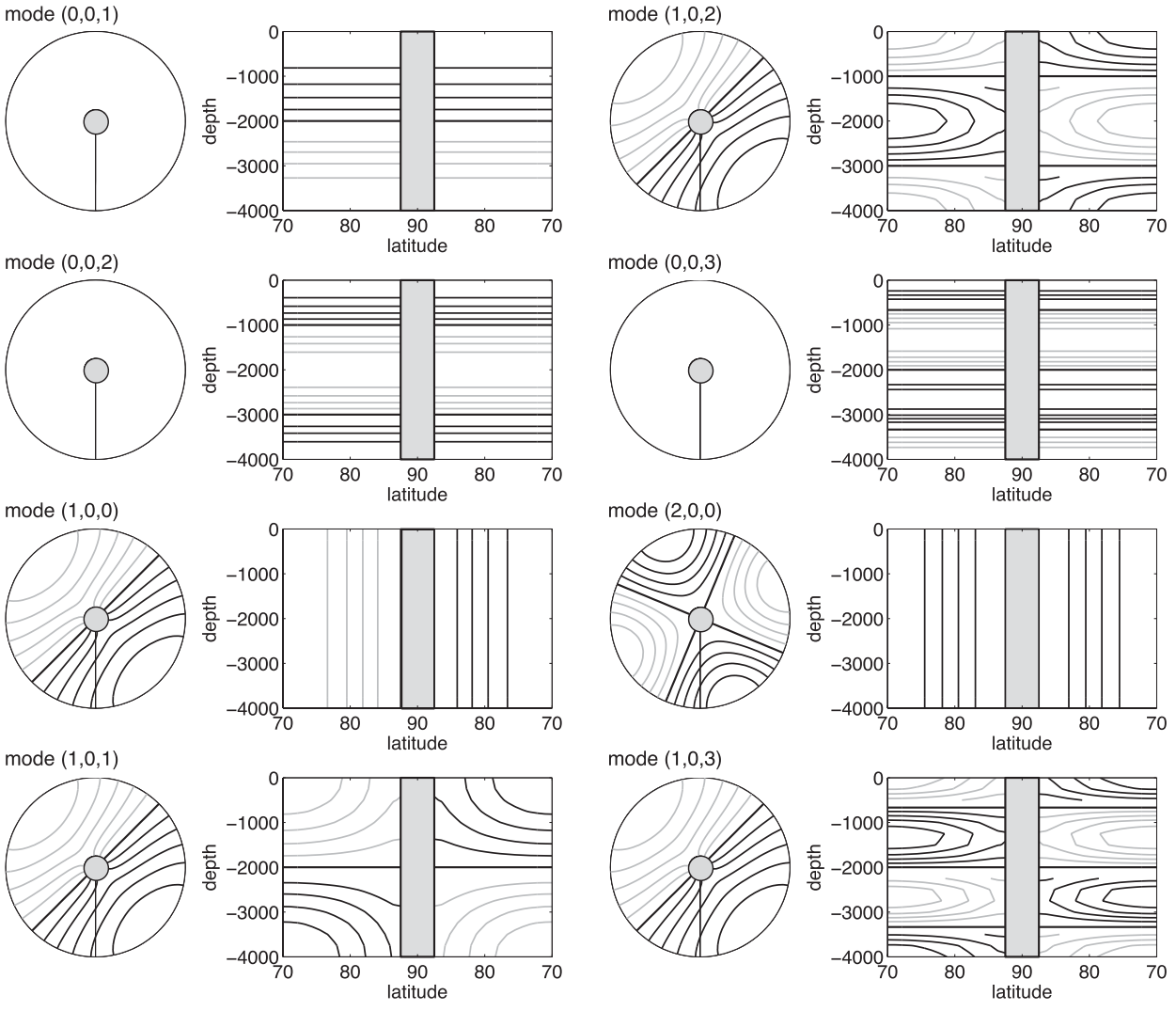

FIG. 1. Spatial salinity pattern at the surface (circles) and in a vertical section (rectangles) of the eight least damped modes. Land is shaded gray, negative contours are plotted in gray, and the zero contour is thick. The amplitude of the modes is arbitrary.

using the Jacobi–Davidson QZ method (Sleijpen and van der Vorst 1996), and order the eigenvalues $\sigma = \sigma_r + i\sigma_i$ according to the magnitude of their real part (the growth rate). For each eigenvalue σ, there is a corresponding eigenvector $\mathbf{x} = \mathbf{x}_r + i\mathbf{x}_i$ according to (3). Oscillatory modes appear as complex conjugate pairs of eigenvalues and the time dependence of these oscillatory modes can be represented by the function

$$\Phi(t) = e^{\sigma_r t}(\mathbf{x}_r \cos\sigma_i t - \mathbf{x}_i \sin\sigma_i t).$$

Propagation of the pattern can therefore be determined by plotting $\mathbf{x}_r$ (which represents the spatial pattern of the mode at $t = 0$) and $\mathbf{x}_i$ (which represents the spatial pattern of the mode at $t = -\pi/2$).

3. Circular basin with a polar island

To illustrate the methodology as described above, we will start with the idealized case of a circular basin with a polar island with $\theta_s = 70°$N and $\theta_n = 87.5°$N. No-slip and zero salt flux conditions are applied along the northern and southern boundaries; periodic conditions apply along the eastern and western boundaries. We use a 90×16 grid over the ocean region and there are 16 evenly spaced levels in the vertical.

a. Stationary salinity modes

For the zero forcing case ($\Delta S = 0$), the flow is motionless [$(u, v, w) = 0$] and the salinity field is determined by the equation

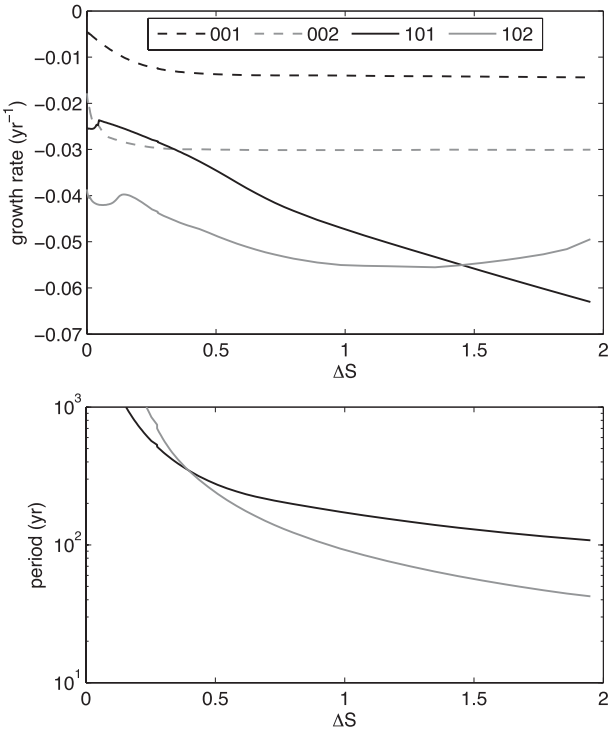

FIG. 2. Growth rates and periods of four of the modes as the forcing ΔS increases.

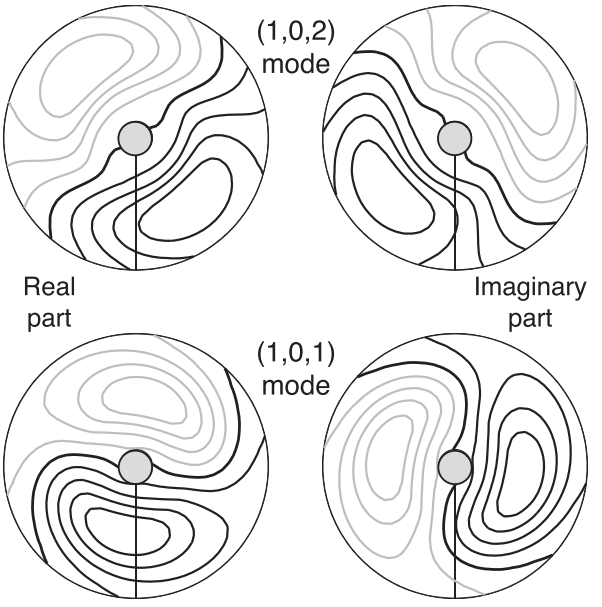

FIG. 3. Real and imaginary parts of (top) the oscillatory (1, 0, 2) mode and (bottom) the (1, 0, 1) mode for $\Delta S = 1.62$. Format is as in Fig. 1.

$$\frac{\partial S}{\partial t} = \frac{K_H}{r_0^2 \cos\theta}\left[\frac{\partial}{\partial\phi}\left(\frac{1}{\cos\theta}\frac{\partial S}{\partial\phi}\right) + \frac{\partial}{\partial\theta}\left(\cos\theta\frac{\partial S}{\partial\theta}\right)\right] + K_V\frac{\partial^2 S}{\partial z^2},$$

with boundary conditions

$$z = -D, 0 \quad : \quad \frac{\partial S}{\partial z} = 0$$
$$\theta = \theta_s, \theta_n \quad : \quad \frac{\partial S}{\partial\theta} = 0,$$

and we apply periodic boundary conditions in the ϕ direction; that is,

$$S(0,\theta,z) = S(2\pi,\theta,z); \quad \frac{\partial S}{\partial\phi}(0,\theta,z) = \frac{\partial S}{\partial\phi}(2\pi,\theta,z).$$

The general solution can be found by separation of variables,

$$S(\phi,\theta,z,t) = \Phi(\phi)\Theta(\theta)Z(z)e^{\sigma t},$$

and as the problem is homogeneous, it has only nontrivial solutions for specific values of σ. The eigenvalue problem can be reduced to that of a one-point boundary eigenvalue problem, as is shown in the appendix. Although this problem can be solved analytically in terms of Legendre functions, we have chosen to solve it numerically (details are provided in the appendix). For this case, it turns out that all the eigenvalues σ are real and negative; hence, the internal modes are stationary. We can label the internal modes according to the indices (n, m, l), where each index indicates the number of zeros of the eigenfunction in the domain, with n representing the number of zeros in the zonal direction, m the number in the meridional direction, and l the number of zeros with depth.

In Table 2, results for the growth rates of the (n, m, l) modes are provided for two values of K_V. For $K_V = 2.3 \times 10^{-4}$ m^2 s^{-1}, the middle column in Table 2 provides the growth rates as computed numerically from the two-point boundary eigenvalue problem, as in the appendix. The third column in Table 2 shows the values as directly computed by solving the eigenvalue problem (3) from the discretized model in section 2a. The agreement of both values provides a check on the eigenvalue computation through (3). We find that the growth rate of the modes depends slightly on the size of the polar island (cf. the $\theta_n = 87.5°$N and $\theta_n = 90.0°$N results). In addition, the growth rates are also dependent on the value of K_V, for example when K_V is decreased from 2.3×10^{-4} to 1.0×10^{-4} m^2 s^{-1}, the (0, 0, 3) mode switches from being the sixth to the third-least damped mode.

Spatial patterns for the eight least damped modes are shown in Fig. 1 for the case where $\theta_n = 87.5°$N and $K_V = 2.3 \times 10^{-4}$ m^2 s^{-1}. Note that the amplitudes of the patterns are arbitrary. The patterns do not change as θ_n and

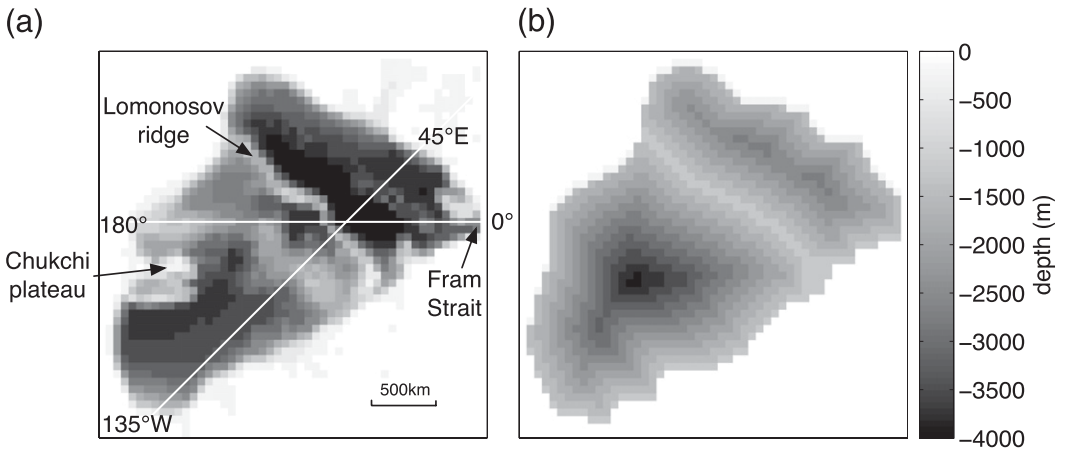

FIG. 4. Map showing (a) the real bathymetry of the Arctic Basin and (b) an idealized bathymetry with a ridge. The white lines indicate the sections used in Fig. 13.

K_V vary. The two least damped modes, (0, 0, 1) and (0, 0, 2), have exactly the same growth rates as in the North Atlantic basin used in the normal mode calculations of Dijkstra (2006), and these are also independent of the size of the polar island. This is because the growth rates for the $n = 0, m = 0$ modes only depend on the vertical diffusion time scales. Modes with $m = 1, 2, \ldots$ have very negative growth rates (i.e., they are highly damped).

b. Mode merging due to nonzero forcing

To study the emergence of oscillatory modes, an idealized salinity pattern is applied as the surface boundary condition. Salinity is restored to a sinusoidal profile with amplitude ΔS; that is,

$$f(\phi,\theta) = -\cos\pi\frac{\theta-\theta_s}{\theta_n-\theta_s},$$

with saline water near the polar island and fresher waters along the outer edge of the basin. This causes an anticlockwise circulation pattern to develop. Starting from $\Delta S = 0$, we increase the forcing of the flow and determine steady circulation states versus ΔS. We then diagnose the freshwater flux, which is needed to maintain this steady state and determine the linear stability of the steady state under prescribed flux conditions. This procedure is similar to that in Dijkstra (2006).

Figure 2a shows how the growth rates of four of the modes that appear in the circular basin change with increasing strength of the forcing. All the modes have a negative growth rate, indicating that the steady equilibrium solution is stable. The various (0, 0, l) modes have growth rates that are almost constant as forcing increases (after an initial adjustment) while the other modes show a strong dependence of growth rate on forcing strength. Due to the circular symmetry of the basin, there are two copies of each stationary (1, 0, l) mode, each having the same spatial pattern under a rotation; that is, the corresponding real eigenvalue has an algebraic multiplicity of 2. The two copies of each mode merge for very small values of ΔS, giving rise to an oscillatory mode. The periods of two of these oscillatory modes are plotted in Fig. 2b.

The mode with the shortest period as ΔS increases is the (1, 0, 2) mode. The propagation of the mode can be visualized using the real and imaginary parts, shown in the top panel of Fig. 3. The imaginary part is the pattern at time $t = -\pi/2$ and the real part is the pattern at time $t = 0$. The anomalies move anticlockwise (eastward), in the same direction as the background flow. The mode with the second shortest period is the (1, 0, 1) mode. It propagates clockwise (westward) against the background flow; the real and imaginary parts are shown in the bottom panel of Fig. 3. In the case of the (1, 0, 2) mode [the (1, 0, 1) mode], the phase velocity of the mode is smaller (larger) than the background velocity, leading to an eastward (westward) propagating salinity anomaly pattern. The difference in the phase speed of both modes

TABLE 3. Growth rates (yr^{-1}) of the least damped modes for the flat-bottomed Arctic Basin.

n	m	l	Growth rate
0	0	1	-4.5042×10^{-3}
0	0	2	-1.7844×10^{-2}
1	0	0	-3.7244×10^{-2}
0	0	3	-3.9506×10^{-2}
1	0	1	-4.1749×10^{-2}
1	0	2	-5.5089×10^{-2}
0	0	4	-6.8659×10^{-2}
1	0	3	-7.6751×10^{-2}

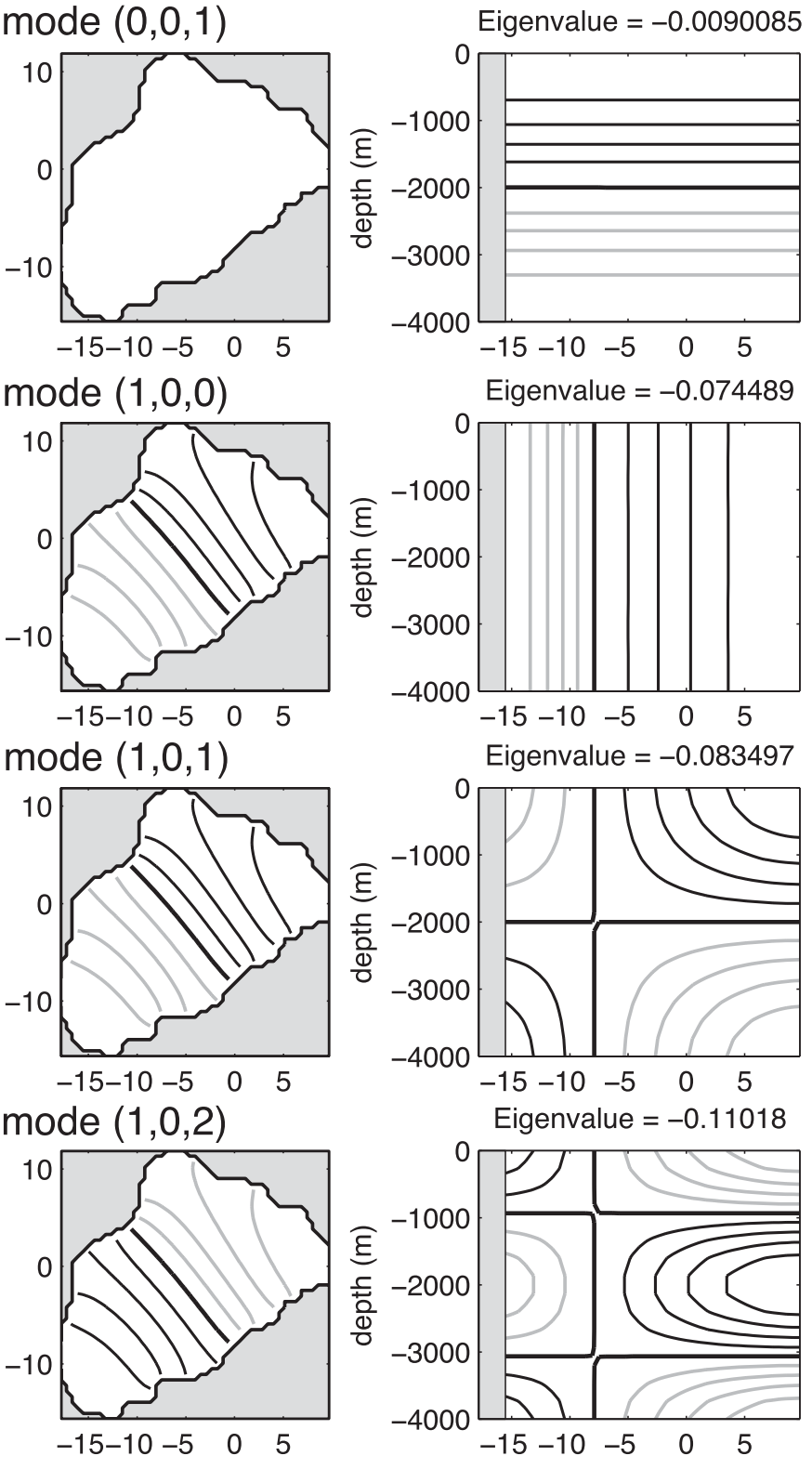

FIG. 5. Spatial salinity patterns (left) at the surface and (right) in a vertical section of the first, third, fifth, and sixth least damped modes in the flat-bottomed Arctic Basin under zero forcing. Format is as in Fig. 1.

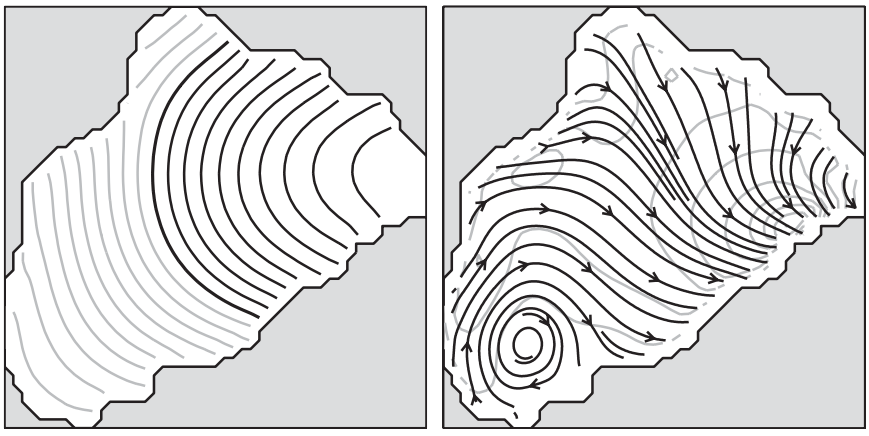

FIG. 6. (left) Surface salinity forcing with negative contours in gray and (right) the resulting surface circulation with streamlines (black with arrows) and speed contours (gray). Surface speeds reach a maximum of just under 20 cm s^{-1} for $\Delta S = 1$.

is related to their different vertical structures; this is analogous to free baroclinic Rossby waves where the phase speed also decreases with increasing vertical wavenumber.

4. Arctic Basin

We now apply the ideas from the previous section to more realistic Arctic Ocean Basin configurations. The topography of the Arctic Basin is shown in Fig. 4. There are shallow seas around much of the Arctic and these are closed in the model topography. To avoid the problems associated with the convergence of the grid at the poles, the earth's rotation vector is rotated so that it is at the equator. The Arctic Basin is then also positioned at the equator. This is equivalent to rotating the grid so that the poles of the grid are at the equator; however, the implementation is simpler since only the Coriolis parameter has to be changed, from $2\Omega \sin\theta$ to $2\Omega \cos\theta \cos\phi$. We use a 51×51 grid over the Arctic Basin, which gives a resolution of approximately 60 km in the horizontal. Again, there are 16 evenly spaced vertical layers, each 250 m thick.

a. Basin geometry

First, we consider only the effects of the basin geometry on the stability of the salinity-driven flows and study the case of a flat bottom. For $\Delta S = 0$, the growth rates of the salinity modes are listed in Table 3. For simplicity, n is the number of zeros along the long axis of the basin (i.e., along the 135°W–45°E line in Fig. 4a), m is the number of zeros in the short axis, and l is the number of zeros with depth, as before. These modes, for which the salinity patterns are shown in Fig. 5, can be compared to the kinds of modes seen in the circular basin. Once again, the least damped modes are the (0, 0, 1) and (0, 0, 2) modes, followed by the (1, 0, 0) mode. The (0, m, 0) modes are also strongly damped in this case, as in the circular basin. Note that, because there is no longer any circular symmetry, the algebraic multiplicity of each of the modes is now equal to 1 (i.e., unlike in the case with a circular basin, there is only one copy of each mode).

We again apply a simplified surface salinity forcing, of which the pattern of $f(\phi, \theta)$ is shown in Fig. 6a. Here, the regions nearest to the Atlantic inflow area are saltier. Once again, ΔS represents the amplitude of the forcing, that is, the difference between the saltiest water at the Atlantic inflow region and the freshest water on the opposite side of the basin. This salinity-forcing pattern results in a surface circulation pattern shown in Fig. 6b. While this circulation does not represent the Arctic Circumboundary Current, it does mimic the anticyclonic circulation in the interior of the Arctic Basin (Nøst and Isachsen 2003), making it adequate for a first estimate of the internal modes.

As the forcing strength ΔS is increased, oscillatory modes once again appear, of which one has a period in the multidecadal range. This oscillatory mode is created through the merging of two different stationary modes: the (1, 0, 1) mode and the (1, 0, 2) mode. The real and imaginary parts of the eigenvalues of these two modes are shown in Fig. 7. Both modes are stationary for small ΔS; thus, the imaginary parts of their eigenvalues are zero (Fig. 7b). For very small values of ΔS, the eigenvalues of the modes are difficult to follow; in fact, for some steps the model could not find the modes at all, leading to gaps in the curves in Fig. 7. However, once the modes were reacquired by the model, they are recognizable by their spatial patterns as the (1, 0, 1) and (1, 0, 2) modes.

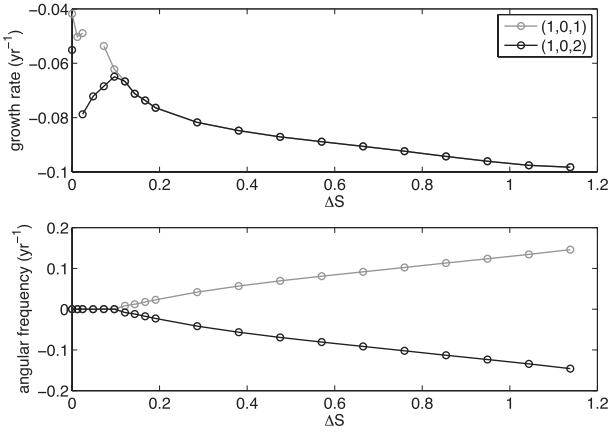

FIG. 7. Growth rate and period of the (1, 0, 1) and (1, 0, 2) modes as the amplitude of the forcing ΔS increases for the flat-bottomed Arctic Basin. The merger of the two modes creates an oscillatory mode.

As the two modes merge, the imaginary parts of their eigenvalues become nonzero and the real parts of their eigenvalues become identical. That is, their eigenvalues are of the form $\sigma_r \pm i\sigma_i$. This is the same type of merger that occurs in modes as studied in Dijkstra (2006). The pattern of propagation is shown in Fig. 8, where we can see that anomalies develop in the Canada basin and propagate across the pole toward the Atlantic inflow region. The period of this mode is in the multidecadal range and its dependence on the forcing strength ΔS is plotted and shown later (Fig. 12).

An estimate of ΔS can be obtained by considering the range of salinity values observed in the real Arctic according to the *World Ocean Atlas 2005* (Antonov et al. 2006). Averaging the salinity over the upper 250 m (the thickness of the model layers), and excluding the shelf seas (which are not included in the model), gives a ΔS value of approximately 2.

b. Bottom topography

Circulation in the Arctic is greatly influenced by the large ridges that stretch across the basin, and the pattern and propagation of internal modes depend on the background circulation. Intricate topography is not possible in the model, but we make an approximation of the Lomonosov Ridge, as shown in Fig. 4b.

Figure 9 shows that the stationary modes that appear under zero forcing ($\Delta S = 0$) in this case differ from the modes seen in the previous two cases. The two least damped modes, for example, are a kind of (0, 0, 1) mode where the negative anomaly at depth is found on one side of the ridge or the other. Similarly, the patterns for many of the more damped modes are not as easily classified as in the flat-bottomed Arctic case as some of them appear to have different (n, m, l) patterns in each of the two subbasins.

The same surface salinity forcing pattern (Fig. 6) is used as in the flat-bottomed Arctic case, with salty water near the Atlantic inflow region. The resulting steady surface circulation for $\Delta S = 1$ is shown in Fig. 10. Comparing this pattern to the circulation pattern in the case with no bottom topography (Fig. 6b), we can see that the ridge causes circulation in the basin to be separated into two parts, one on either side of the ridge, as is the case

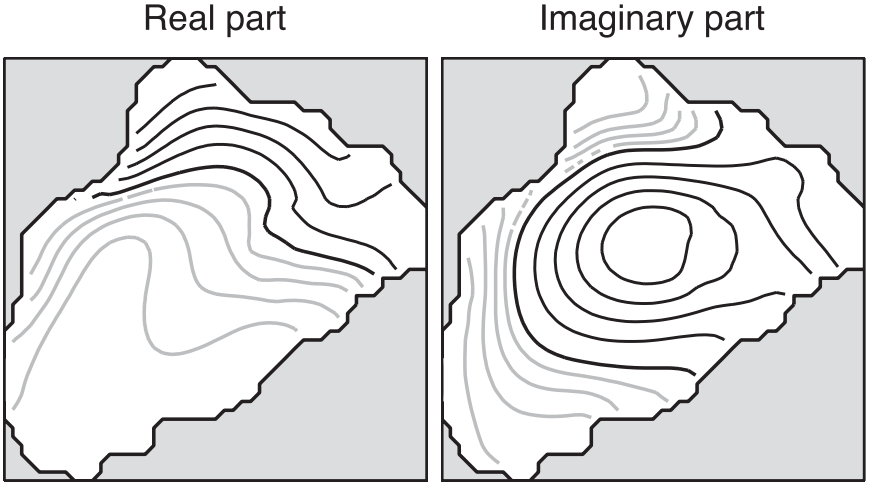

FIG. 8. Real and imaginary parts of the oscillatory mode with the shortest period for the flat-bottomed Arctic Basin for $\Delta S = 1.14$. Format is as in Fig. 1. The propagation of the mode can be visualized as follows: the imaginary part shows the mode at $t = -\pi/2$, and the real part shows the mode at $t = 0$. Another quarter of a period later, at $t = \pi/2$, the mode is given by the negative of the imaginary part, and at $t = \pi$ by the negative of the real part.

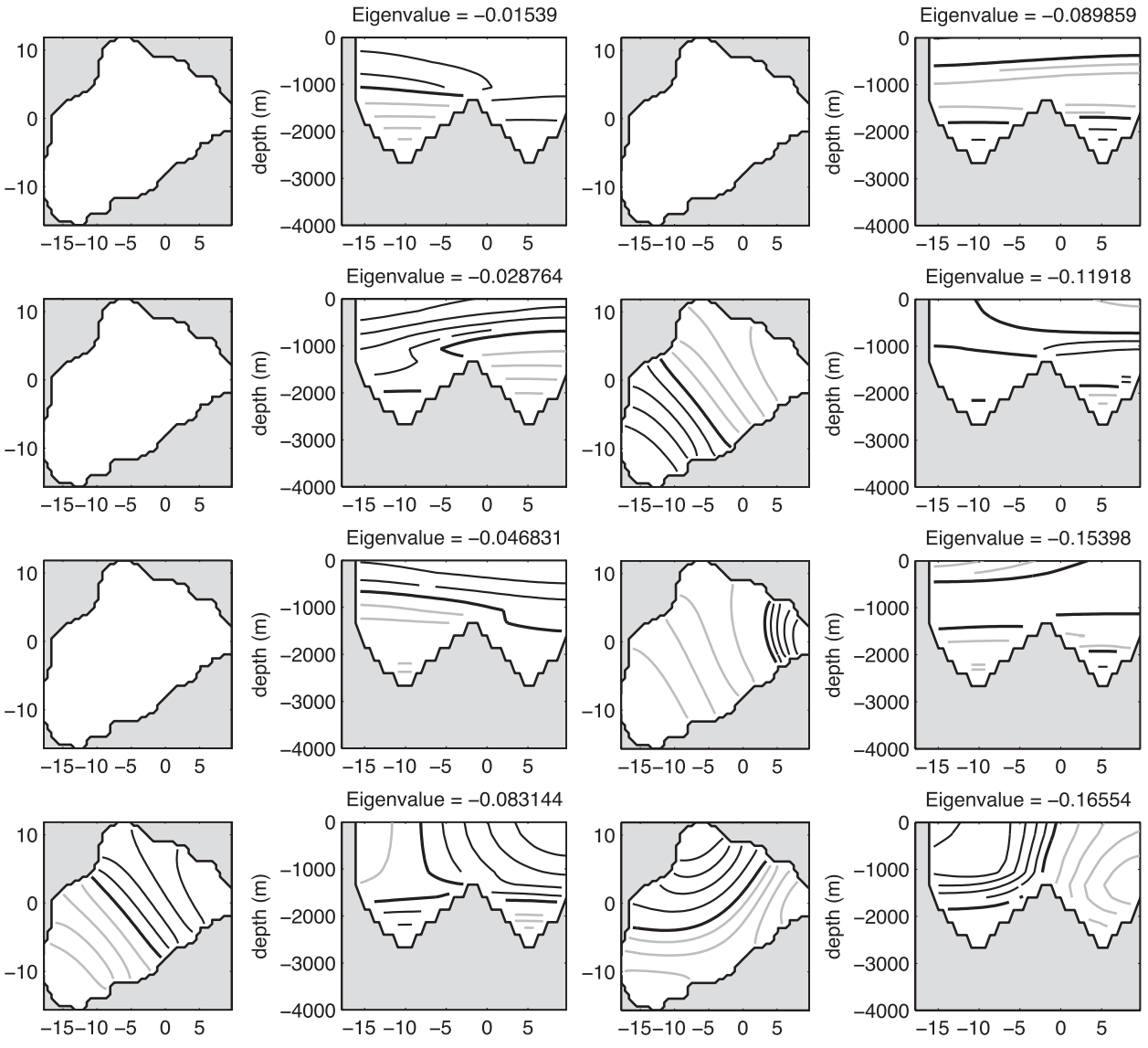

FIG. 9. Spatial salinity patterns (left),(right center) at the surface and (left center),(right) in a vertical section of the eight least damped modes under zero forcing in the Arctic Basin with a ridge. Format is as in Fig. 1.

for the real Arctic Ocean. However, making the model circulation resemble the circulation in the real Arctic more closely would require intricate bottom topography (and also a representation of Atlantic inflow), in which case finding solutions with the pseudoarclength continuation method becomes difficult. We are therefore restricted to simplified versions of the topography (and no Atlantic inflow).

As in the flat-bottomed case, there is one oscillatory mode with a multidecadal period. The spatial pattern and period of this mode are similar to the flat-bottomed case. The real and imaginary parts of the mode are plotted in Fig. 11 and the dependence of the period on ΔS is plotted in Fig. 12. The main difference in the spatial pattern is that the salinity anomalies do not penetrate so strongly toward the Atlantic side of the ridge, showing that the idealized ridge is blocking the propagation of the mode. The presence of the ridge also decreases the growth rates of the modes compared to the flat-bottomed case, indicating that topography has a stabilizing influence on the flow, similar to the results of Winton (1997).

The spatial pattern of the oscillatory modes depends on the background circulation. Circulation in the real Arctic is largely controlled by bathymetry, whereas in the model Arctic it depends more on the surface forcing (which is unrealistic). An attempt to make the model circulation appear more like the real one (by making three peaks in salinity forcing to mimic the circulation in the three main

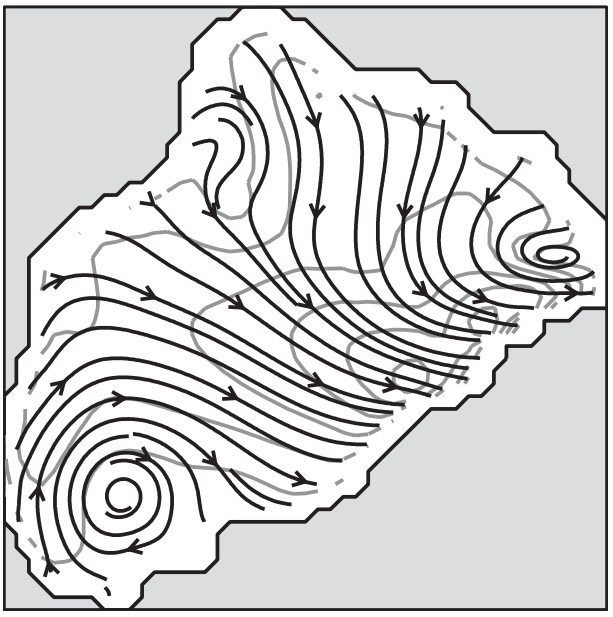

FIG. 10. Surface circulation for the Arctic Basin with a ridge. Streamlines are shown in black, and gray contours indicate velocity. Surface velocities reach a maximum of about 10 cm s^{-1} for $\Delta S = 1$.

Arctic basins) resulted in an oscillatory mode with a time scale very similar to those already shown here. The spatial pattern was deformed by the surface forcing but the mode still propagated in a manner similar to the two cases shown above. This shows that the multidecadal oscillatory mode is reasonably robust in the model Arctic.

c. Comparison with the CM2.1 MSSA mode

The exact time scale of the oscillatory modes found in the idealized model depends on the amplitude of the surface forcing (Fig. 12) and also on the values of the mixing coefficients, in particular K_V (te Raa and Dijkstra 2002; Huck et al. 2001); however, it remains in the multidecadal range. The spatial patterns of the modes do not change much with small variations in these parameters. Instead of precisely tuning the periods of the oscillatory modes here to the time scale of the oscillatory Multi-Channel Singular-Spectrum Analysis (MSSA) mode in the GFDL CM2.1 as found in Frankcombe et al. (2010), we compare the spatial pattern of the modes over one oscillation period.

Figure 13 shows Hovmöller plots along the two longitudinal sections marked with the white lines in Fig. 4a: the first is along 180° through the pole and then along 0° (parallel to the model grid) and the second is along 135°W through the pole and then along 45°E (approximately along the long axis of the basin). From these Hovmöller plots, we can see some similarities between the spatial patterns. First, comparing the patterns from the simple model with and without a ridge, we can see that the presence of the ridge affects the propagation of the anomalies toward the Atlantic side of the basin. Second, if we compare the pattern from the coupled model with the patterns from the simple model along the 180°–0° line, we see the same general pattern of propagation.

However, there are also some discrepancies between the spatial patterns of both modes, which become more clear when looking along the 135°W–45°E line. In the GFDL CM2.1 the anomaly propagates southward away from the pole (in both directions), but in the simple model it propagates from the Canada Basin over the pole toward the Atlantic inflow region. This difference can be attributed to the absence of the Chukchi Plateau

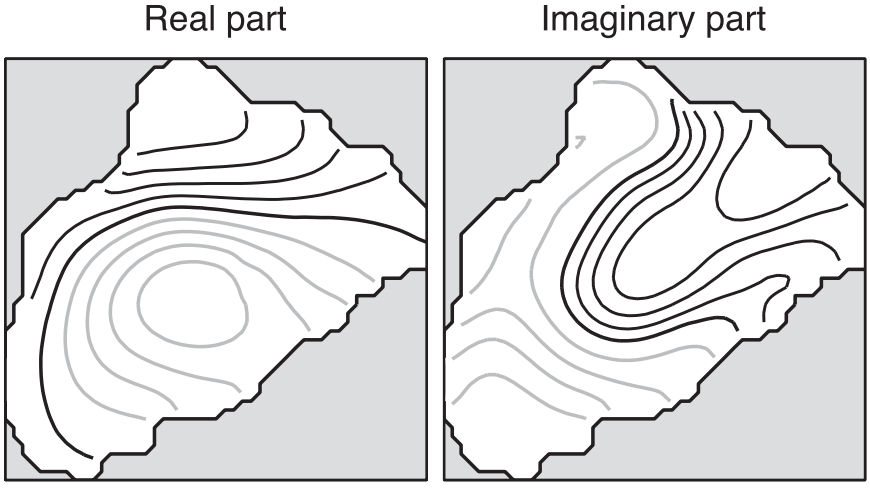

FIG. 11. Real and imaginary parts of the least damped oscillatory mode in the Arctic Basin with a ridge for $\Delta S = 0.75$. Format is as in Fig. 1, and the propagation is as described in Fig. 8.

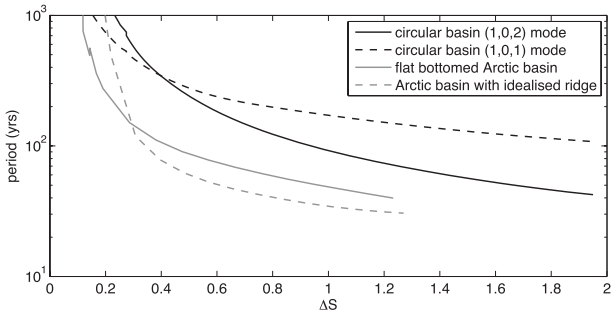

FIG. 12. Periods of the oscillatory modes vs ΔS for the different cases considered.

in the simple model. In the GFDL CM2.1 the pattern appears to propagate from close to the Chukchi Plateau toward the pole, with anomalies then spreading southward through the Canada Basin. In the simple model the anomalies propagate from the Canada Basin itself. More sophisticated bathymetry would have to be implemented in the model to investigate how the presence of the Chukchi Plateau, as well as the shallow seas along the Russian shelf, would affect the spatial pattern of the mode.

5. Summary and discussion

In this paper, we have investigated the internal modes of the variability of salinity-driven flows in idealized Arctic basins. These modes can be determined by solving the linear stability problem of a particular salinity-driven steady state under prescribed flux conditions. As a control parameter, we have used the parameter ΔS, the amplitude of the salinity forcing.

For $\Delta S = 0$, the modes are stationary (real eigenvalue) in all configurations investigated. The easiest modes to understand are those on the circular basin with a polar island. These are the solutions to the anisotropic Laplace equation on a near-polar circular sector and their meridional structure is given by Legendre functions (see the appendix). The different modes for this case can still be recognized for the flat-bottom Arctic Basin and also in the case with bottom topography, where the spatial structures of each mode are deformed by the presence of topography.

When the forcing ΔS is increased, many of the modes remain stationary and damped (i.e., negative, real eigenvalues). However, merging occurs for some modes, which leads to oscillatory modes (nonzero imaginary parts). The periods of these modes eventually reach multidecadal values under a reasonable salinity contrast over the basin. The mechanism of propagation here is the ''saline'' Rossby wave, which is induced by the background gradient in the salinity. This is analogous to the ''thermal'' Rossby waves discussed in Dijkstra (2006), induced by a background temperature gradient, and ordinary Rossby waves that propagate due to the background gradient of potential vorticity. The modes intrinsically propagate westward (just like ordinary Rossby waves) but they can be arrested by the eastward background flow; eastward-propagating anomalies are therefore also possible. This is illustrated by the eastward-propagating (1, 0, 2) mode and the westward-propagating (1, 0, 1) mode in the circular basin (Fig. 3). It seems that oscillatory modes with multidecadal periods are a robust feature of our model Arctic. Under the most realistic configuration considered here, and taking into account the simplified bathymetry in our model, the pattern of the least damped oscillatory mode tends to look like the MSSA mode of the multidecadal variability that was found in the GFDL CM2.1 (Frankcombe et al. 2010).

The growth rate for all modes found is negative; hence, for the modes to be observable they would have to be excited. Growth rates depend strongly on the background circulation since modes can only grow if the salinity anomalies transported by the circulation lead to circulation anomalies that reinforce the original salinity anomalies. Since the background circulation in our idealized Arctic is not realistic, we cannot expect to have realistic growth rates.

Now, as we have no thermal and momentum forcing in the model, as well as no parameterization for sea ice, the patterns of the modes should be interpreted as occurring below the Arctic halocline. This is consistent with the appearance of the mode from the GFDL CM2.1, which was found below the halocline in that model. It has previously been shown (Frankcombe et al. 2009) that damped oscillatory modes can be excited by the inclusion of noise in the system. The most plausible mechanism for the excitation of the internal modes in this kind of situation is variability in the inflow of the Atlantic water. Once excited, the internal variability would cause circulation changes in the Arctic, altering heat and freshwater storage.

The model Arctic considered in this paper is highly idealized. Improvements on this model would be necessary in order to make a closer comparison with the results from the GFDL CM2.1. In addition, in order to study the exchange between the Arctic and the North Atlantic, the next step would be to make a model coupling the two basins. This would allow us to study the influences of the internal oscillations found in the North Atlantic on the Arctic, and vice versa.

Acknowledgments. This research was sponsored by the Netherlands Organization of Scientific Research (NWO)

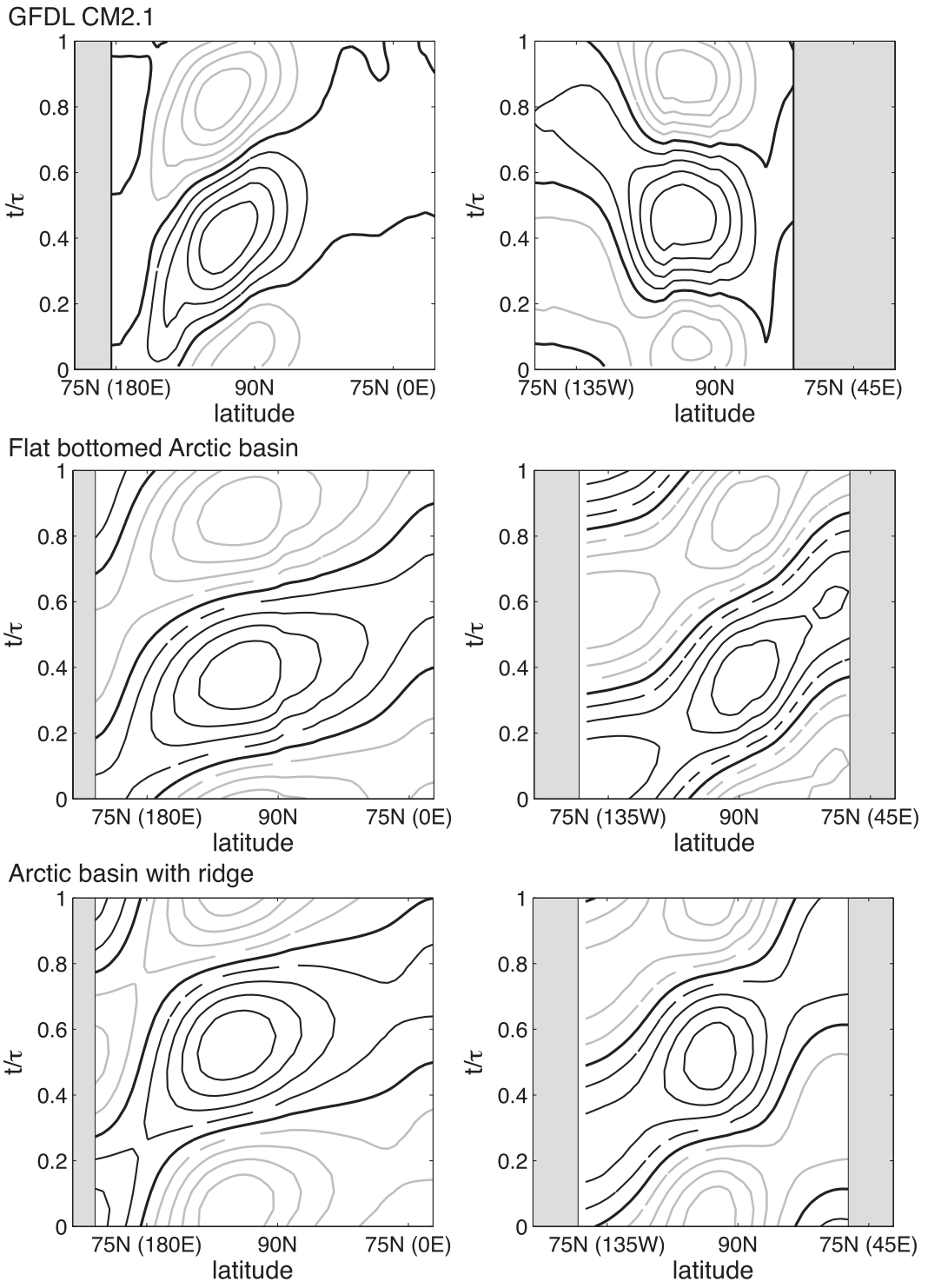

FIG. 13. Hovmöller plots of (top) the propagation of the salinity anomaly normalized by the period τ across two longitudinal sections from the GFDL CM2.1 coupled model ($\tau \approx 100$ yr), (middle) the oscillatory mode of the flat-bottomed Arctic Basin (from Fig. 8, $\tau \approx 43$ yr), and (bottom) oscillatory mode of the Arctic Basin with a ridge (from Fig. 11, $\tau \approx 42$ yr). The longitudinal sections (shown in Fig. 4) are along (left) 180°–0° and (right) 135°W–45°E.

through its Earth and Life Sciences Division under Project ALW854.00.037.

APPENDIX

Analytical Solution

For the case of a circular basin with a polar island, the general solution can be found by separating the variables,

$$S(\phi, \theta, z, t) = \Phi(\phi)\Theta(\theta)Z(z)\Gamma(t),$$

which leads to four problems:

$$\frac{\Phi''}{\Phi} = -\mu^2, \tag{A1a}$$

$$\Theta''\cos\theta = \Theta'\sin\theta - \Theta\left(\chi\cos\theta - \frac{\mu^2}{\cos\theta}\right), \tag{A1b}$$

$$\frac{Z''}{Z} = (\chi + \lambda)\frac{K_H}{K_V r_0^2}, \quad \text{and} \tag{A1c}$$

$$\frac{\Gamma'}{\Gamma} = \lambda\frac{K_H}{r_0^2}, \tag{A1d}$$

where μ, χ, and λ are separation constants. The boundary conditions become

$$Z'(-D) = Z'(0) = 0 \quad \text{and} \tag{A2a}$$

$$\Theta'(\theta_s) = \Theta'(\theta_n) = 0. \tag{A2b}$$

The solutions to (A1a) and (A1c) are sinusoids while the solution to (A1d) is an exponential. Using the boundary conditions, we can solve for the separation constants:

$$\mu = 0, 1, 2, \ldots$$

$$-(\chi + \lambda) = (l\pi)^2\frac{K_V r_0^2}{K_H D^2}, \quad l = 0, 1, 2, \ldots$$

So our solutions to (A1a), (A1c), and (A1d) are

$$\Phi = C_1\sin(\mu\phi) + C_2\cos(\mu\phi), \quad \mu = 0, 1, 2, \ldots$$

$$Z = C_3\cos\left(\frac{\pi l}{D}z\right), \quad l = 0, 1, 2, \ldots, \quad \text{and}$$

$$\Gamma = C_4 e^{\lambda K_H/r_0^2 t},$$

where C_1–C_4 are constants.

The solution to (A1b) may be found by substituting $x = \sin\theta$ into the equation, which then becomes

$$\Theta''(1 - x^2) - 2x\Theta' + \Theta\left(\chi - \frac{\mu^2}{1 - x^2}\right) = 0.$$

Introducing $\chi = \nu(\nu + 1)$, this equation reduces to the standard form of the Legendre equation. Instead of solving this equation analytically, we solve (A1b) by discretizing the equation with boundary conditions (A2b) on a one-dimensional grid with $M = 16$ points and solving the resulting algebraic eigenvalue problem numerically using a standard library [Numerical Algorithms Group (NAG)] routine.

REFERENCES

Alvarez-Garcia, F., M. Latif, and A. Biastoch, 2008: On multidecadal and quasi-decadal North Atlantic variability. *J. Climate,* **21,** 3433–3452.

Antonov, J. I., R. A. Locarnini, T. P. Boyer, A. V. Mishonov, and H. E. Garcia, 2006: *Salinity*. Vol. 2, *World Ocean Atlas 2005,* NOAA Atlas NESDIS 62, 182 pp.

Belkin, I. M., S. Levitus, J. I. Antonov, and S.-A. Malmberg, 1998: ''Great Salinity Anomalies'' in the North Atlantic. *Prog. Oceanogr.,* **41,** 1–68.

De Niet, A. C., F. W. Wubs, A. D. Terwisscha van Scheltinga, and H. A. Dijkstra, 2007: A tailored solver for bifurcation studies of ocean–climate models. *J. Comput. Phys.,* **277,** 654–679.

Dijkstra, H. A., 2005: *Nonlinear Physical Oceanography*. 2nd ed. Springer, 532 pp.

——, 2006: Interaction of SST modes in the North Atlantic Ocean. *J. Phys. Oceanogr.,* **36,** 286–299.

Eden, C., and T. Jung, 2001: North Atlantic interdecadal variability: Oceanic response to the North Atlantic Oscillation (1865–1997). *J. Climate,* **14,** 676–691.

Frankcombe, L. M., H. A. Dijkstra, and A. von der Heydt, 2009: Noise-induced multidecadal variability in the North Atlantic: Excitation of normal modes. *J. Phys. Oceanogr.,* **39,** 220–233.

——, A. von der Heydt, and H. A. Dijkstra, 2010: North Atlantic multidecadal climate variability: An investigation of time scales and processes. *J. Climate,* **23,** 3626–3638.

Huck, T., G. K. Vallis, and A. Colin de Verdiére, 2001: On the robustness of the interdecadal modes of the thermohaline circulation. *J. Climate,* **14,** 940–963.

Nøst, O. A., and P. E. Isachsen, 2003: The large-scale time-mean ocean circulation in the Nordic seas and Arctic Ocean estimated from simplified dynamics. *J. Mar. Res.,* **61,** 175–210.

Polyakov, I. V., and M. A. Johnson, 2000: Arctic decadal and interdecadal variability. *Geophys. Res. Lett.,* **27,** 4097–4100.

——, R. V. Bekryaev, G. V. Alekseev, U. S. Bhatt, R. L. Colony, M. A. Johnson, A. P. Maskshtas, and D. Walsh, 2003a: Variability and trends of air temperature and pressure in the maritime Arctic, 1875–2000. *J. Climate,* **16,** 2067–2077.

——, and Coauthors, 2003b: Long-term ice variability in Arctic marginal seas. *J. Climate,* **16,** 2078–2085.

——, and Coauthors, 2004: Variability of the intermediate Atlantic water of the Arctic Ocean over the last 100 years. *J. Climate,* **17,** 4485–4497.

Sleijpen, G. L. G., and H. A. van der Vorst, 1996: A Jacobi–Davidson iteration method for linear eigenvalue problems. *SIAM J. Matrix Anal. Appl.,* **17,** 410–425.

Stroeve, J., M. M. Holland, W. Meier, T. Scambos, and M. Serreze, 2007: Arctic sea ice decline: Faster than forecast. *Geophys. Res. Lett.,* **34,** L09501, doi:10.1029/2007GL029703.

te Raa, L. A., and H. A. Dijkstra, 2002: Instability of the thermohaline ocean circulation on interdecadal timescales. *J. Phys. Oceanogr.,* **32,** 138–160.

Thompson, D. W. J., and J. M. Wallace, 2001: Regional climate impacts of the Northern Hemisphere annular mode. *Science,* **293,** 85–89.

Venegas, S. A., and L. A. Mysak, 2000: Is there a dominant timescale of natural climate variability in the Arctic? *J. Climate,* **13,** 3412–3434.

Vinje, T., T. B. Loyning, and I. Polyakov, 2002: Effects of melting and freezing in the Greenland Sea. *Geophys. Res. Lett.,* **29,** 2129, doi:10.1029/2002GL015326.

Visbeck, M., E. P. Chassignet, R. G. Curry, T. L. Delworth, R. R. Dickson, and G. Krahmann, 2003: *The North Atlantic Oscillation: Climatic Significance and Environmental Impact*. *Geophys. Monogr.,* Vol. 134, Amer. Geophys. Union, 279 pp.

Winton, M., 1997: The damping effect of bottom topography on internal decadal-scale oscillations of the thermohaline circulation. *J. Phys. Oceanogr.,* **27,** 203–208.